1-16-2010

Timing of present and future snowmelt from high elevations in northwest Montana

Bonnie Jean Gillan
University of Montana - Missoula

Joel T. Harper
University of Montana - Missoula

Johnnie N. Moore
University of Montana - Missoula, johnnie.moore@umontana.edu

Recommended Citation

Gillan, B. J., J. T. Harper, and J. N. Moore (2010), Timing of present and future snowmelt from high elevations in northwest Montana, Water Resour. Res., 46, W01507, doi:10.1029/2009WR007861.

Timing of present and future snowmelt from high elevations in northwest Montana

Bonnie J. Gillan,[1] Joel T. Harper,[1] and Johnnie N. Moore[1]

Received 14 February 2009; revised 19 August 2009; accepted 10 September 2009; published 16 January 2010.

[1] The sensitivity of snowmelt-driven water supply to climate variability and change is difficult to assess in the mountain west, where strong climatic gradients coupled with complex topography are sampled by sparse ground measurements. We developed a model which ingests daily satellite imagery and meteorological data and is suitable for areas >1000 km^2, yet captures spatial variability of snow accumulation and melt in steep mountain terrain. We applied the model for the years 2000–2008 to a 2900 km^2 snowmelt-dominated watershed in NW Montana. We found that >25% of the basin's snow water equivalent (SWE) accumulates above the highest measurement station and >70% accumulates above the mean elevation of surrounding SNOTEL stations. Consequently, scaling point measurements of SWE to describe basin conditions could lead to significant misrepresentation of basin snow. Simulations imply that present-day temperature variability causes measures of snowmelt timing to vary by over 4 weeks from year-to-year. Temperature variability causes a larger spread in snowmelt timing in a warmer climate. On average, snowmelt timing occurs 3 weeks earlier in late 21st century projections, with about 25% of future conditions observed today.

Citation: Gillan, B. J., J. T. Harper, and J. N. Moore (2010), Timing of present and future snowmelt from high elevations in northwest Montana, *Water Resour. Res.*, *46*, W01507, doi:10.1029/2009WR007861.

1. Introduction

[2] Snow accumulation and melt dominates the hydrologic cycle of the mountainous western United States, where the annual fraction of stream discharge originating as snow is over 60% [*Serreze et al.*, 1999], and perhaps as high as 75% [*Cayan*, 1996; *Palmer*, 1988]. Winter snowpacks act as natural water storage systems, providing runoff to aquatic and riparian ecosystems, reservoir storage, and agricultural lands in the otherwise dry summer months. By simple reasoning, a warmer climate will result in more precipitation falling as rain and earlier snowmelt runoff, effectively limiting water storage and runoff during the dry season. With estimates of 20th century global warming on the order of 0.74°C, and significantly more warming expected in the 21st century [*Intergovernmental Panel on Climate Change* (*IPCC*), 2007] the fate of the western snowpack is a topic with wide-ranging implications.

[3] Recent awareness of anthropogenic forcing of the Earth's climate has spurred numerous studies of snowmelt hydrology in the western United States that suggest changes due to climate warming have already begun. Several studies indicate a shift toward rain in winter precipitation [*Knowles et al.*, 2006; *Regonda et al.*, 2005], that winter snowpacks have depleted [*Mote*, 2006], that snowmelt is perhaps occurring earlier [*McCabe and Clark*, 2005; *Moore et al.*, 2007; *Stewart et al.*, 2005], and that flood risks are changing [*Hamlet and Lettenmaier*, 2007]. One attribution modeling study attests that up to 60% of these climate-related trends are associated with human-caused warming [*Barnett et al.*, 2008].

[4] Understanding of climate-induced changes in the mountain snowpack, however, is poorly constrained by actual measurements. The federally run network of measurement locations (snow course and Snow Telemetry sites (SNOTEL)) was not designed to address research questions such as the impacts of climate change, but was established to generate index measurements for water forecasts (NRCS Data Collection Network Fact Sheet, available at http://www.wcc.nrcs.usda.gov/factpub/sntlfct1.html.). Consequently, most data are collected below the upper tree line at locations that do not adequately sample the full landscape characteristics of a typical alpine mountain basin [*Bales et al.*, 2006; *Molotch and Bales*, 2006]. Topography, vegetation, wind, and microclimatic effects cause large variability in the distribution of snow at scales varying from meters to kilometers [*Deems et al.*, 2006; *Elder et al.*, 1991]; this variability exists at much finer scales than our available data sets can effectively sample [*Bales et al.*, 2006]. Interpolations of SNOTEL point data often do not yield accurate measures of snow distribution because of the nonrepresentative location of these sites [*Fassnacht et al.*, 2003; *Molotch and Bales*, 2005]. Furthermore, SNOTEL time series are short, extending back only several decades for the longest records. Snow course sites on the other hand, have substantially longer records but low temporal time resolution with measurements taken monthly or sub monthly at best. Data sets drawn from snow courses for trend analysis use 1 April snow water equivalent (SWE) as a proxy for the maximum annual SWE, an assumption that has been shown to underestimate peak SWE by an average of 12% [*Bohr and Aguado*, 2001]. Further-

[1]Department of Geosciences, University of Montana, Missoula, Montana, USA.

0043-1397/10/2009WR007861$09.00

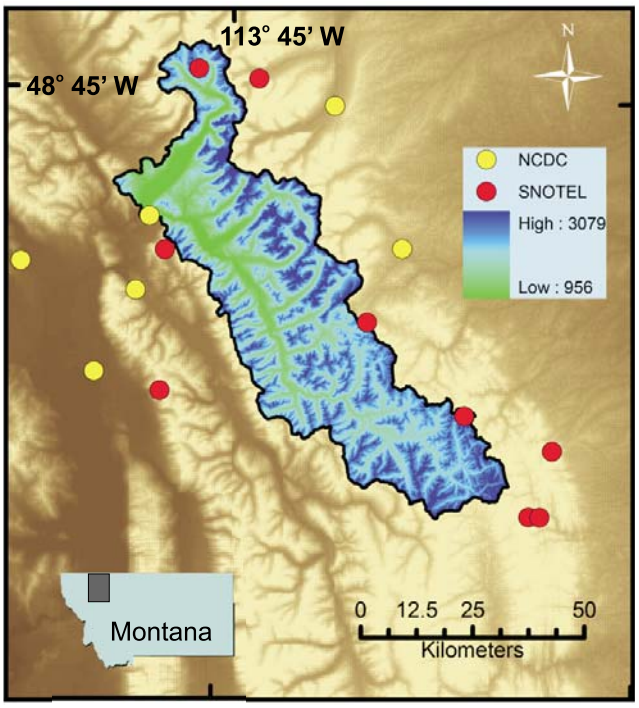

Figure 1. Middle Fork Flathead Basin outline and surrounding meteorological stations. Shading from blue to green shows basin elevation.

more, SWE at these sites is often strongly affected by changes in the local vegetation and physical site conditions, sometimes making it difficult to interpret long-term trends in SWE [*Julander and Bricco*, 2006].

[5] The current state of the situation is that we have good reason to anticipate climate driven change to snow water resources, and we have some degree of evidence that this change is underway. However, we lack sufficient data to fully assess ongoing change or project future change of the mountain snowpack. The mountains of western Montana exemplify this problem. Analysis of existing data implies that in recent decades Montana's snowpack has become smaller and melted earlier [*Mote*, 2006], and this has perhaps caused increased frequency and duration of wildfires [*Westerling et al.*, 2006]. The mountainous area of western Montana is approximately 125,000 km^2 and contains 89 SNOTEL sites and 267 snow course sites. Most SNOTEL sites also serve as snow course locations effectively improving the quality of data, but reducing the total number of points at which snow is monitored. With approximately 270 independent points, western Montana has one SWE monitoring location per 460 km^2 on average. However, only 89 of these are measured at a frequency greater than once per month. Hence, a sparse network of measurements which are difficult to scale upward forms the basis for our understanding of the distribution and potential changes in SWE.

[6] The goals of this study are twofold. First, we characterize the spatial distribution of snow accumulation across one of the largest mountainous basins of northwestern Montana. We characterize the spatial variability of SWE across the mountain range scale in areas otherwise unmeasured by ground observations. Through a modeling approach, we combine snow products from the Moderate Resolution Imaging Spectroradiometer (MODIS) with ground based meteorological measurements to quantify the snow accumulation during 9 years. Second, we perform numerical simulations on our modeled snowpacks to investigate the sensitivity of snowmelt timing to temperature variability across this large basin, and its response to warming predicted by downscaled climate models.

2. Methods

2.1. Study Area and Model Domain

[7] The Middle Fork of the Flathead River (MF) basin of western Montana covers an area of over 2900 km^2 (Figure 1). The basin's elevations span over 2000 m in relief, with steep gradients extending from 956 m at the valley floor to over 2900 m at many peaks. The MF basin borders the western side of the continental divide. The climate is primarily driven by Pacific coastal systems with occasional interruptions by continental air masses from the north and east. At Badger Pass, the highest measurement station (2100 m), the average annual temperature and precipitation in the last decade were 2.3°C and 1.23 m, respectively. Conversely, West Glacier, the lowest measurement station (961 m), annually averaged 6.7°C and 0.72 m of precipitation (data from SNOTEL site and remote automated weather station).

[8] The Flathead River basin is a major tributary of the upper Columbia River. The MF River drains the Great Bear Wilderness and the Waterton-Glacier International Peace Park. The basin remains largely untouched by dams, infrastructure, and land use changes such as timber harvest and agriculture, making it particularly useful in determining the role that climate can play in snow and snowmelt runoff. The valley floors and lowlands are heavily vegetated and forested primarily with Douglas-fir (*Pseudotsuga menziesii*) and ponderosa pine (*Pinus ponderosa*). Blocky peaks of the Precambrian Belt Super Group rise above the tree line at ~2450 m.

[9] Daily mean temperature data exists for a total of 15 surrounding meteorological stations (Figure 1 and Table 1). These include SNOTEL stations operated by the Natural Resources Conservation Service offering temperature and SWE data, and six National Climate Data Center meteorological stations providing only temperature data. This research uses select attributes from these data sources as inputs to a numerical model of the MF basin (described below). The basin topography is represented by a digital elevation surface (DEM), slope surface, and aspect surface obtained in 30 m grid spacing from the U.S. Geological Survey (USGS). These surfaces were resampled to 500 m grid spacing so that the 12,300 pixels representing the MF basin have spatial correspondence to MODIS snow products. An area surface was created in order to compensate for sloping topography represented by the 500 m pixels. Modeling and simulations are carried out on the MF basin alone, but interpolations utilize a larger rectangle surrounding the basin to eliminate boundary effects, and to offer a larger palette from which to draw information.

2.2. Snow Accumulation Model

[10] We developed a snow accumulation model (SAM) to quantify the spatial distribution of wintertime SWE for the MF basin over the period 2000–2008. Unfortunately, the

Table 1. Meteorological Stations in and Around the MF Basin[a]

Station Name	Elevation (m)	Cell Aspect (deg)
	SNOTEL	
Badger Pass	2103	332
Emery Creek	1326	336
Flattop Mtn	1921	56
Many Glacier	1494	158
Noisy Basin	1841	354
Pike Creek	1808	173
Dupuyer Creek	1753	345
Mt. Lockhart	1951	173
Waldron	1707	214
	NCDC	
West Glacier	961	268
Hungry Horse	963	164
Creston	896	177
Whitefish	945	331
St. Mary	1390	22
East Glacier	1465	230

[a]SNOTEL sites are used for temperature and SWE; NCDC sites are used for temperature. Cells are the 500 × 500 m cells used for modeling.

SWE product available from the National Operational Hydrologic Remote Sensing Center (NOHRSC) is unsuitable for our work because (1) the product does not offer a sufficiently long period of record, (2) extremely high relief in portions of the MF basin is poorly represented by the 1 × 1 km resolution, and (3) the product is based on distributed energy balance, but sparse meteorological observations and complex topography make this questionable for the MF basin. Our SAM uses satellite imagery to indicate the location of snow, and meteorological data to indicate melt conditions. Time integration of this melt yields the total accumulated snowpack across the landscape. This summation represents all melted snow, but not necessarily a snowpack existing on the ground at one time, especially at lower elevations where snow can be highly transient. At the high elevations where winter melt is minor, however, our summation is roughly equal to peak SWE, providing there are no significant accumulation events during the melt season. Our model uses a similar "inverse melt" approach to *Molotch* [2009] for estimating snow accumulation from satellite imagery and meteorological data. Our choice of MODIS data has the advantage of high time resolution, but disadvantage of poor space resolution relative to LANDSAT imagery used by *Molotch* [2009]. Further details and limitations of SAM are described below.

2.2.1. MODIS Snow Cover

[11] MODIS refers to the instruments flying onboard the Terra and Aqua Earth Observing System platforms, launched 2000 and 2002, respectively, which produce a snow covered area (SCA) product. We processed MODIS data with the HDF-EOS to GeoTiff Conversion Tool, removing distortion due to the sinusoidal projection of the data and aligning MODIS pixels with our MF framework [*Taaheri et al.*, 2007]. Products used in this study include daily and 8 day composite 500 m resolution tiles [*Hall et al.*, 2006]. The 8 day SCA product identifies pixels greater than 50% covered as snow, and offers a maximum extent of snow over the interval. This product is temporally coarse and does not offer sub pixel information. A method sufficiently robust to estimate the fraction of snow within a pixel was developed in 2004 [*Salomonson and Appel*, 2004], and has subsequently been applied by NASA to all daily MODIS data. The daily fractional snow covered area (FSCA) product offers daily updates and subpixel resolution, but is highly limited by cloud cover.

[12] With the ability to distinguish a single pixel as 1% to 100% snow covered, the apparent resolution of the daily product is 25 m^2 out of 2500 m^2. However, *Salomonson and Appel* [2004] found that the computed fraction of snow cover in a pixel has a mean absolute error of up to 10%. Overall MODIS SCA product errors have been assessed by comparison to in situ measurements [*Ault et al.*, 2006; *Simic et al.*, 2004; *Zhou et al.*, 2005], other remotely sensed products, as well as other MODIS products [*Hall and Riggs*, 2007; *Salomonson and Appel*, 2006]. The clear-sky absolute accuracy of the MODIS products in determining snow/no snow has been estimated at ~93%, but found to vary by land cover type and snow condition [*Hall and Riggs*, 2007]. Recent improvements in the MODIS cloud mask have reduced cloud errors in the reprocessed version 5 data, which are used in this study. Snow and canopy reflectance models have been used to develop indices that improve the discrimination of the original MODIS snow-mapping algorithm between snow-covered and snow-free forests [*Klein et al.*, 1998]. Our basin varies from forest cover to treeless alpine terrain and the snow cover product is known to have poorer accuracy in closed canopy evergreen forest [*Hall and Riggs*, 2007]. The error values reported by *Hall and Riggs* [2007] are similar to those found in the MF basin, based on comparison of 267 MODIS (MOD10A2) snow cover products collected during the snow seasons of a 6 year period (2000–2005) with information from six SNOTEL stations and over 1000 ground based measurements [*Bleha and Harper*, 2007]. Further, *Bleha and Harper* [2007] found that omission errors with this nonfractional snow cover product are most common when SWE is less than 5 cm, likely because a small fraction of the pixel is covered by snow when SWE is low.

2.2.2. Cloud Fill

[13] We developed a method to fill in the SCA beneath clouds in the daily products that are minimally obscured by clouds. We chose not to employ the methods for cloud fill used by previous studies [e.g., *Cline and Carroll*, 1999; *Molotch et al.*, 2004; *Parajka and Blöschl*, 2008] because these methods do not result in subpixel resolution or were not possible in the MF basin due to lacking ground observations required by those methods.

[14] Here, we use daily FSCA and 8 day SCA Terra data products in conjunction to fill pixels in cloud-obscured areas (Figure 2). For each 8 day SCA product we determined the percent snow cover in all elevation bands and then computed the elevation snow cover gradient (% covered/per meter of elevation) (Figure 2c). In some images, a ceiling is present where the SCA is 100% for all higher-elevation bands. The elevation snow gradient was used to interpolate to cloud obscured pixels in the daily FSCA tiles. We used the Linear Lapse Rate Adjustment (LLRA) method [*Dodson and Marks*, 1997] to spatially interpolate values on the DEM. With this method, values for each cell in the elevation grid are transformed to a datum elevation using the elevation snow gradient. Inverse distance interpolation is then used to estimate missing values. The elevation snow gradient is then used to retransform values back to original elevations. Daily

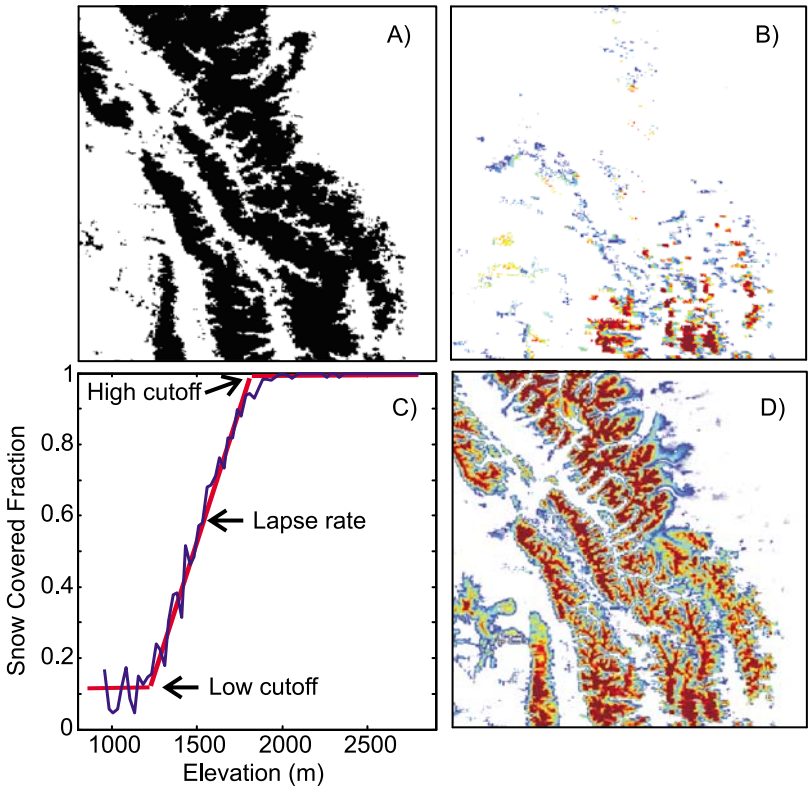

Figure 2. Construction of daily snow cover product from combination of MODIS daily and MODIS 8 day products. Data from 2006 shown as example. (a) MODIS 8 day snow cover product with black showing snow cover. (b) MODIS daily fractional snow cover product. Comparison of data density with Figure 2a indicates that much of the image is obscured by clouds. (c) Snow cover lapse rate and cutoffs determined manually from snow cover versus elevation for a single 8 day product. (d) Cloud-filled fractional snow cover product based on information in snow cover versus elevation plot shown in Figure 2c.

maps greater than 90% cloud covered were considered too poorly constrained to fill and the previous day's map was used in its place. This process produced daily fractional snow cover tiles for the years 2000 to 2008.

2.2.3. Snowmelt

[15] The new fractional snow cover product is input into an enhanced temperature index melt model incorporating incoming shortwave radiation (Figure 3). The temperature-index melt method often outperforms distributed energy balance models at the catchment scale [*Hock*, 2003]. We incorporate solar radiation dependence to improve representation of spatial and seasonal variability of melt rates. Melt rates are largely determined by radiation, which in turn, is dependent on atmospheric conditions and topography. Here, we assume only the effects of topography (namely slope, aspect, and shading) drive radiation transfer. The SAM employs an additive melting approach that has been shown to improve snowmelt model performance by separating temperature-dependent and temperature-independent terms [*Pellicciotti et al.*, 2005]. The melting equation uses daily time steps so that the melt, M, is calculated as

$$\begin{aligned} M &= \alpha T + \beta I T > T_c \\ \mathrm{M} &= 0\mathrm{T} \leq \mathrm{T}_c. \end{aligned} \tag{1}$$

Here, I is potential clear-sky direct solar radiation, T is temperature, α and β are coefficients of the temperature factor and solar radiation factor, respectively. We take T_c = 1°C to account for accuracy errors in temperature sensors and the fact that melting does not necessarily occur at the freezing point [*Kuhn*, 1987].

[16] Temperatures from 15 stations (Figure 1 and Table 1) were distributed across the basin using a locally calculated lapse rate with LLRA spatial interpolation method for temperatures [*Dodson and Marks*, 1997]. Hourly values of the potential clear-sky direct solar radiation were calculated for each cell as a function of top of atmosphere solar radiation [*Hock*, 1999], and these values were summed for a daily total. The actual radiation received at any point on the snowpack may often be less, but is unaccounted for by our model. Our calculations do account for topographic shading of cells from the sun. We calculated α and β locally as 0.003 $\mathrm{md^{-1}\,C^{-1}}$ and 1.66 $\times$ 10^{-6} $\mathrm{m^2\ mW^{-1}\ d^{-1}}$, respectively, by way of a multiple linear regression. This regression was performed using SNOTEL melt and temperature data from the two sites within the MF basin and our calculated solar radiation from the pixels that contain those stations. Although solar radiation is input explicitly, this does not give our melt term an energy balance component. When combined with the solar radiation factor, the entire radiation component becomes a "radiation index" giving the total melt the signature of the seasonal influence of the sun.

[17] We consider only the generation of snow meltwater and do not model present or future runoff to streams dictated by soil and vegetation processes [e.g., *Bavay et al.*, 2009].

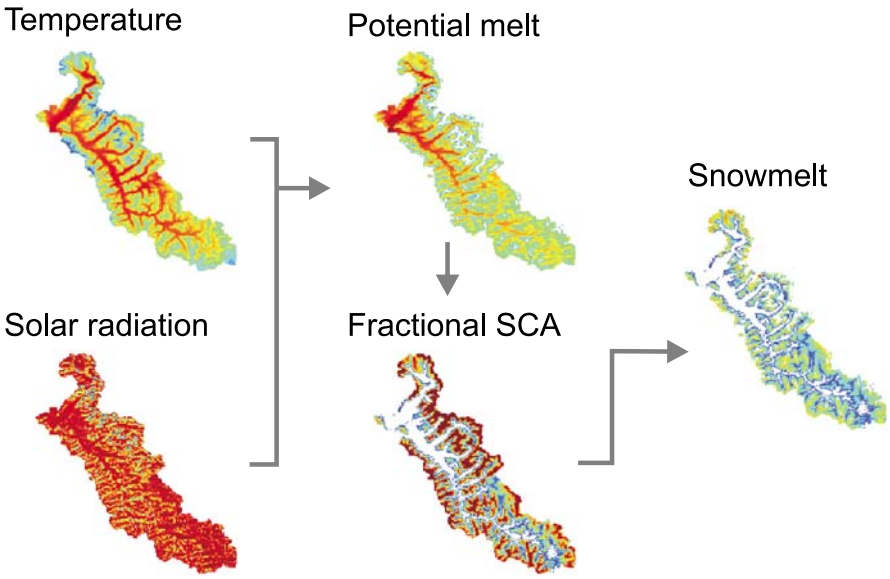

Figure 3. Schematic overview of the snow accumulation model (SAM). Temperature and solar radiation are input to the model, and "potential melt" is calculated. Potential melt is multiplied by the fractional SCA resulting in the actual snowmelt for each pixel on a given day. Data from 2006 shown as example.

Our model is run for the first 250 days of the year. Limiting runs to this period captures the spring snowmelt season, but reduces computational expense. The actual period during which snowmelt was generated from the basin was less than 147 days, and closer to 110 days in most years.

2.2.4. Model Assumptions

[18] We invoke numerous assumptions and simplifications to implement this high time/space resolution model at the mountain range scale. Our representation of snow considers subgrid snow accumulation processes only if they are properly represented by the fractional snow cover value for each pixel. Our representation of melt may be more problematic since we interpolate data over a large area and input data are biased toward low/middle elevations. To test the sensitivity of our results to the distribution of input data, we performed a data removal experiment whereby we eliminated 1–3 stations, chosen randomly, from the interpolation. The inclusion of fewer stations resulted in more snow modeled at higher elevations and had a larger effect in high-snow years than low-snow years (Figure 4). Dropping 1–2 stations produced just 0.3% more snow, however, including 12 out of the 15 stations had a bigger impact, resulting in up to 3.7% more snow at high elevation. From this analysis it does not appear that adding more low/middle elevation stations would substantially change or improve results, but clearly more information from high elevations is needed to remove potential elevation bias.

[19] We stress that our assumptions and simplifications are numerous and the impact on results is not quantifiable since a truly independent (observational) data set is unavailable for comparison: the need to model would be negated if it was possible to collect these data. While we believe our results provide the best available information regarding the distribution of snow across this region, we also believe that care must be taken in accepting all components of the results. Performance of the model is discussed further in section 3.1.

2.3. Repeated Melt Simulations

[20] We simulated melt of our accumulated snow at high elevations, which is assumed to represent a standing snowpack at time of peak SWE. We define "high elevation" as above 1760 m, the mean elevation of SNOTEL sites. 2001 and 2008 were selected as advantageous focus years because they are the lowest- and highest-snow years, respectively, in our modeled results. Based on Flattop SNOTEL, these are also the years with the greatest and least peak SWE of the last nine years, with 2001 being the lowest on record. At Flattop, 2008 accumulated 113% of the 30 year average snowfall, while 2001 totaled just 66%. We use the same additive melting technique as in the SAM, but vary temperatures according to two experiments, one designed to investigate current natural variability of climate, and one designed to investigate future climate warming.

[21] In our variability experiments we make the assumption that yearly temperature characteristics and precipitation are not independent of each other, and that each year is unique. In other words, a low-snow year such as 2001 is generated and melted by a seasonal temperature that is unique in terms of natural noise frequency and magnitude, and wholly different from the temperature that accompanied the 2008 high-snow year. Hence, available random weather generators based on long-term statistics, although commonly used for simulating typical variability, are not applicable in this case. Instead, we attempt to replicate the temperature noise signature inherent to a specific year and snowpack. Our synthetic temperatures retain the magnitude, frequency and duration of warm and cold events, while conserving the original seasonal trend.

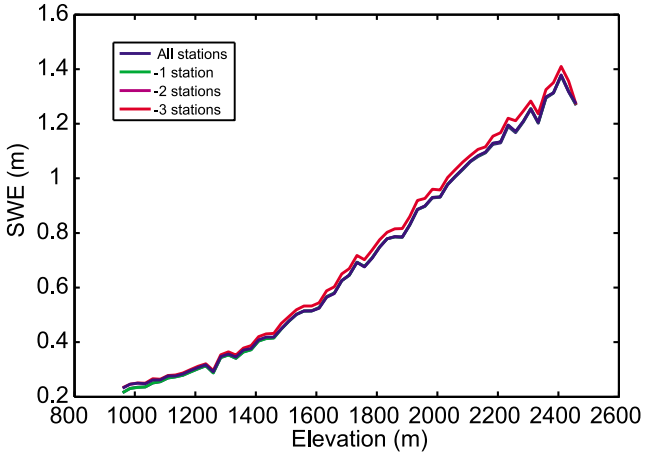

Figure 4. Example results from data removal experiment showing modeled snow water equivalent (SWE) based on inclusion of differing numbers of meteorological stations. Data shown are from 2008 (highest-snow year) and represent the largest change to modeled SWE from dropping 1–3 stations. Not all lines are visible because they plot on top of each other. Results imply that including more low-elevation stations would have minimal benefit. However, all stations used in the analysis are from low-to-middle elevation; high-elevation stations are needed to avoid a bias that becomes more apparent with higher elevation.

[22] Temperatures from the 15 stations are analyzed for days spanning the spring season (days 30–250) for three traits: seasonal trend, daily departure, and event magnitude. The seasonal trend for the spring season is approximated by a cubic best fit to data. The seasonal trend is used as a point of reference and is not input directly as a temperature for simulation. Daily departure describes the magnitude of difference between the daily temperature and the seasonal trend. Event magnitude describes warm and cold events, lasting one to six days, which compose the bulk of natural temperature noise. Event magnitude contains the amplitude and wavelength of warm and cold events as well as a measure of persistence. Persistence adds to the wavelength of an event, and is defined as the number of days temperature remains within one degree of the previous day's temperature. Using these parameters, synthetic temperatures are created which obey a random depiction of the given rule set thereby reflecting the original temperature's magnitude and frequency of noise, while maintaining the seasonal trend. Temperatures are analyzed with an extra several days at the beginning and end dates of concern to minimize end-member effects. Bounds contain the synthetic temperatures to within 2.5 times the mean standard deviation of the original 15 temperatures from their trends. These 15 resulting seasonal temperatures are distributed across the basin using the same approach described above.

[23] Our variability experiments address two characteristics of climatic noise (Figure 5). Our simulations of "high-

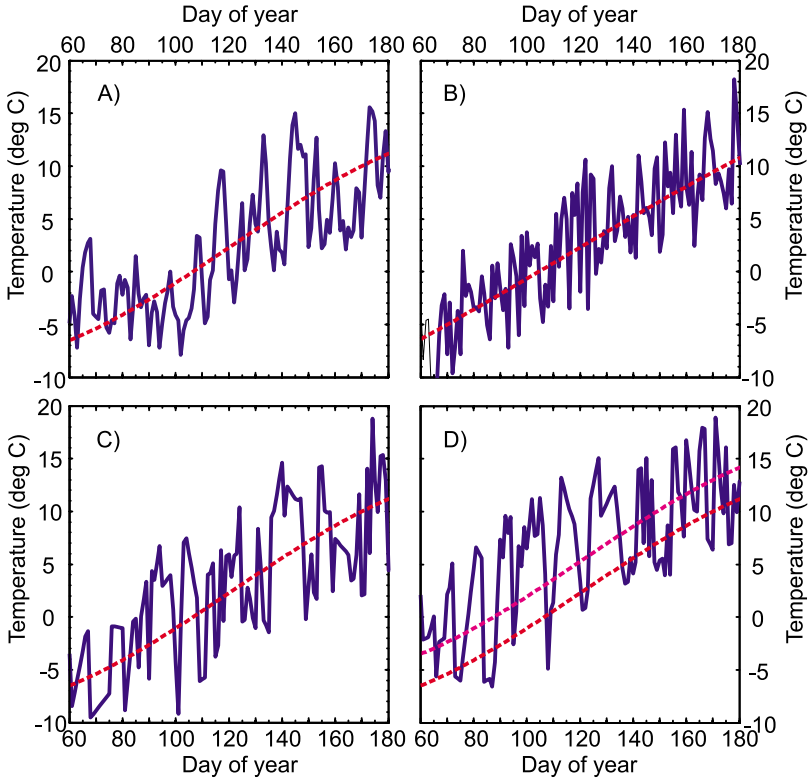

Figure 5. Synthetic temperature variability. (a) Average measured temperature at basin meteorological stations (blue line) with cubic trend (dotted red line). (b) Example of "high-frequency" noise showing randomly generated temperature (blue line) which follows the measured cubic trend (dotted red line). (c) Example of "characteristic noise" showing randomly generated temperature (blue line) following cubic trend (dotted red line). (d) Example of "characteristic noise with warming," showing randomly generated temperature (blue line) and seasonal trend with 3.1°C warming (dotted magenta line).

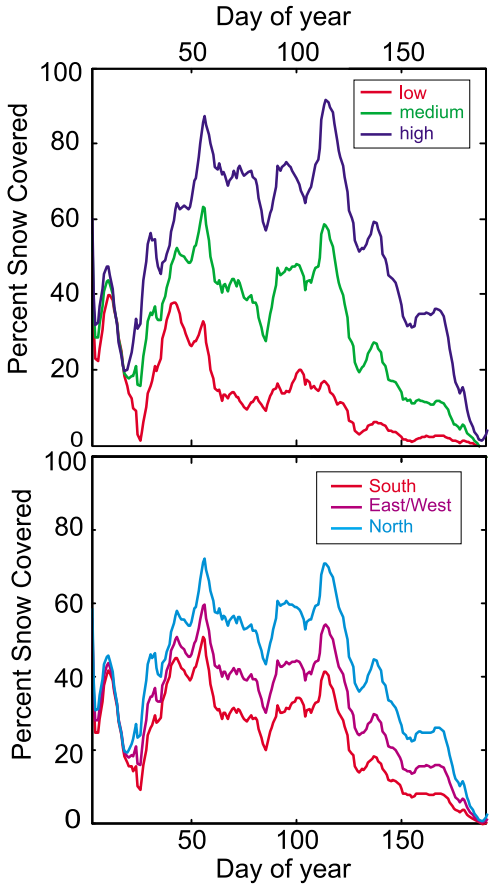

Figure 6. Results of cloud fill for 2005. Snow covered area by (top) elevation and (bottom) aspect. Elevation bands are high, medium, and low, each containing approximately one third of the total basin area. Data have been smoothed with a Savitkay-Golay [*Savitzky and Golay*, 1964] filter to aid visualization while preserving some high-frequency features.

frequency noise" are not meant to be realistic, but to isolate the role of daily temperature departures from the seasonal trend. The synthetic time series of high-frequency noise consists only of a random reorganization of departure from the seasonal trend. Our simulations of "characteristic noise" attempt to mimic reality as they simulate both high-frequency noise and low-frequency events (i.e., multiday warm or cold spells) as present in the actual temperature time series.

[24] Our future warming experiments assume the general character of climate variability remains similar to present-day, but that mean temperatures are changed (Figure 5d). We use downscaled Global Climate Model (GCM) projections at roughly 12 km resolution from the World Climate Research Programme's Coupled Model Intercomparison Project phase 3 (CMIP3) multimodel data set [*Meehl et al.*, 2007]. CMIP3 downscaled climate projections were collected from over 15 climate models run under the IPCC's A1b scenario [*IPCC*, 2007], which describes a linear increase in CO_2 concentration until stabilization in 2100 at 720 ppm. For the years 2070–2099, we binned data according to elevation bands. The ranges of results from different models were used to create normal probability distribution functions for each elevation band. Area weighting the highest probability warming from each elevation band revealed an average annual warming of 3.1°C for the high elevations of the MF. This warming was added to base temperatures and variability simulations were performed as above.

3. Results

3.1. Model Performance

[25] A qualitative assessment of the cloud fill and SCA interpolation scheme can be made by noting the elevations and aspects that exhibit the most and least amounts of SCA (Figure 6). High elevations and north aspects consistently average more SCA than low elevations and southern aspects, respectively. Also, changes in SCA (both accumulation and melting) occur simultaneously among different elevation bands. Further, all nine years of results follow similar spatial and elevation patterns.

[26] Our ability to perform detailed validation of SAM output is inhibited by the fact that no spatially distributed ground-based measurements are available in this rugged mountainous terrain. However, SNOTEL measurements offer the opportunity for a first-order assessment of SAM's output. SNOTEL measurements are point measurements with unique elevation, aspect, and vegetation dependence, and small-scale variability of the mountain snowpack means that the measurements should not be expected to exactly scale to an entire elevation band [*Deems et al.*, 2006; *Molotch and Bales*, 2005; *Elder et al.*, 1991]. All modeled maximum SWE values were within 100% of measured maximum SWE at SNOTEL sites, and three quarters of the values were within 50%. In fact, most SNOTEL values that were less than our modeled results (averaged over elevation) are on south facing pixels, and likewise, most values that were greater than our results are on north facing pixels. Considering the constraints of comparing point measurements of snow with pixel averages, SAM does not appear to produce results that differ significantly from ground measurements.

[27] NOHRSC model output, which begins in 2004, provides a second measure for comparison with the SAM's output [*NOHRSC*, 2004]. Although the NOHRSC product's courser resolution and shorter record limits its utility for detailed comparison, we compared the NOHRSC basin-averaged SWE (on the day of maximum SWE) with the basin-averaged SWE determined by the SAM. Four of the five years were within 85% of NOHRSC modeled results (Table 2). The results differed in the fifth year, 2006, by 33%.

3.2. Basin SWE Distribution

[28] Our study period 2000–2008 sampled a large range of climatic conditions with the total accumulated SWE differing between years by up to 150% (Table 2). The lowest volume of accumulated snow occurred in 2001 with only 1.59×10^9 m^3 of SWE deposited across the basin. The year 2008 had the greatest snow volume with 2.44×10^9 m^3 total accumulated SWE.

[29] Average SWE of accumulated melt from the SAM by elevation closely tracks the basin's distribution of area with elevation (Figure 7). The area of the MF basin is concentrated between 1700 and 2000 m elevation. However, the elevation band that consistently holds the highest volume of SWE is slightly higher in elevation (1800 m–2100 m) (Figure 8). Peak snow volume is consistently at 1984 m, 125 m above the

Table 2. SAM Results and NOHRSC Average Basin SWE on Date of Maximum SWE[a]

Year	Total Basin SWE ($\times 10^9$ m^3)	Total SWE above 1760 m (%)	SWE Lapse 1200–2100 m ($\times 10^{-4}$ m/m)	Average Basin SWE (m)	
				SAM	NOHRSC
2000	1.7616	69.6	6.68	0.5077	-
2001	1.5934	69.0	6.17	0.4593	-
2002	2.0825	70.9	8.00	0.6002	-
2003	1.7138	73.0	7.74	0.4940	-
2004	2.1772	67.9	8.18	0.6275	0.6452
2005	1.9946	77.0	10.41	0.5751	0.5080
2006	1.7396	69.9	7.25	0.5014	0.7493
2007	1.8204	74.0	8.19	0.5247	0.5153
2008	2.4409	69.4	8.30	0.7035	0.8280

[a]SAM, Snow Accumulation Model; NOHRSC, National Operational Hydrologic Remote Sensing Center; SWE, snow water equivalent.

elevation with peak area. Variability in the volume elevation curves corresponds directly to variability in the area elevation curve.

[30] Normalizing SWE by the area at each elevation isolates climate-driven controls on SWE from basin area controls. The distribution of SWE with elevation (Figure 7a) lacks the variability due to basin area (Figure 8), but does exhibit some small repeated irregularities, which are likely due to a repeatable site condition such as slope, shading or local weather. SWE distribution (accumulated melt) with elevation exhibits three distinct phases. All years show SWE following similar shallow linear trends from the lowest elevation in the basin to about 1200 m, where there is an abrupt transition. From 1200 m to about 2000 m, all years show steeper linear trends of varying slope. Above 2000 m, SWE curves mostly roll over to lower slopes and convex shapes. In general, we see three distinct zones of SWE lapse rate trends: (1) a low-elevation zone (bottom–1200 m) with a low, linear lapse rate; (2) midelevation zone (1200 m–2000 m) with a steeper, linear lapse rate; and (3) a high-elevation zone (2000 m–top) that shows flatter, linear to convex SWE trends.

[31] These three phases are illustrated more simply as the average of all nine years (Figure 7b). In the low-elevation zone, representing the basin valley floors, SWE increases at an average slope of 2.61×10^{-4} m/m. SWE follows a linear lapse rate of approximately 7.88×10^{-4} m/m across the midelevation zone that makes up the majority of the mountain fronts and slopes in the basin. In the highest elevation zone, SWE stops increasing rapidly with elevation (and is more variable in shape), taking on a gentler average slope of 4.78×10^{-4} m/m. Inflections in the SWE elevation curve result from the change to lower lapse rates at the highest and lowest portions of the basin. From year-to-year, the MF basin consistently exhibits the differing lapse rates for low/middle/high elevations. The gradient in each zone, however, does show much interannual variability (Figure 7c). The three SWE elevation gradients correspond closely to the basin's mean slope, showing similar inflection points (Figure 7b).

3.3. Timing of Snowmelt

[32] The years 2001 and 2008 had the least and greatest basin wide SWE, respectively. Melt initiated at low elevations and south aspects near the 60th day of both years (Figure 9). As expected, melt occurred earliest at low elevations and south slopes, and progressed upward and northward over the melt season. All study years exhibited this pattern. The elevation and aspect partitioning of melt during the early spring was similar in 2001 and 2008. The high-snow year of 2008, however, had a midspring cold event where no melt occurred anywhere and nearly three weeks of extended melt from middle to high elevation, northerly aspects. The 2001 scenario showed a nonmelt trough similar in timing to that in 2008 but was not as deep, so melt continued even though greatly reduced.

[33] Each melt scenario was run 100 times with random high-frequency (e.g., Figure 5b) and characteristic temperature variability (daily and multiday warm or cold spells, e.g., Figure 5c) on the high-elevation (>1760 m) snowpack of the low-snow year (2001) and high-snow year (2008). Further, each scenario was initiated with present-day temperatures and with temperatures forecast to the period 2070–2099 with 3.1°C of climate warming derived from CMIP3 projections. We have not addressed increased variability in the future scenario with our CMIP3 analysis, effectively making our estimates for the range in timing conservative. Further, future lapse rates may differ from present, and it is unclear how this might impact our findings. Simulation results are analyzed using percentiles of melt, which have been shown to be nonarbitrary and robust descriptors of snowmelt timing [*Moore et al.*, 2007]. Here we compute the day that the 25th, 50th, and 75th percentiles of melt occur. To describe our results, we present the normal probability density function (pdf) describing each suite of 100 simulation runs (Figure 10). All results almost always exhibit normality, with the low-snow future scenario having the greatest variability, and thus the least normality.

[34] There are only small differences in the mean melt timing between the low-snow and high-snow scenarios for both present and future warmer conditions. Under present conditions, the 25th percentiles for the two regimes fall within 1 day of each other (Table 3). The 50th percentile occurs about a week earlier in a low-snow year, and the 75th percentile of melt occurs roughly 2 weeks earlier in the low-snow year. We analyze the amount of variability in melt timing due to temperature variability by discussing the range of days in each melt percentile. We use the term "spread" to describe the range of values extending up to 2 times the standard deviation from the mean on either side. This gives a sense of the total amount of time contained in the most frequent 95% of the set. There is substantially more spread in high-snow years (average of 36 days) compared to low-snow years (25 days), and also spread in future scenarios (35 and 30 days) compared to modern-day scenarios (Table 3). Under both present and future conditions, melt timing occurs on average earlier by about 1–2 weeks in low-snow years compared to high-snow years. However, the spread due to

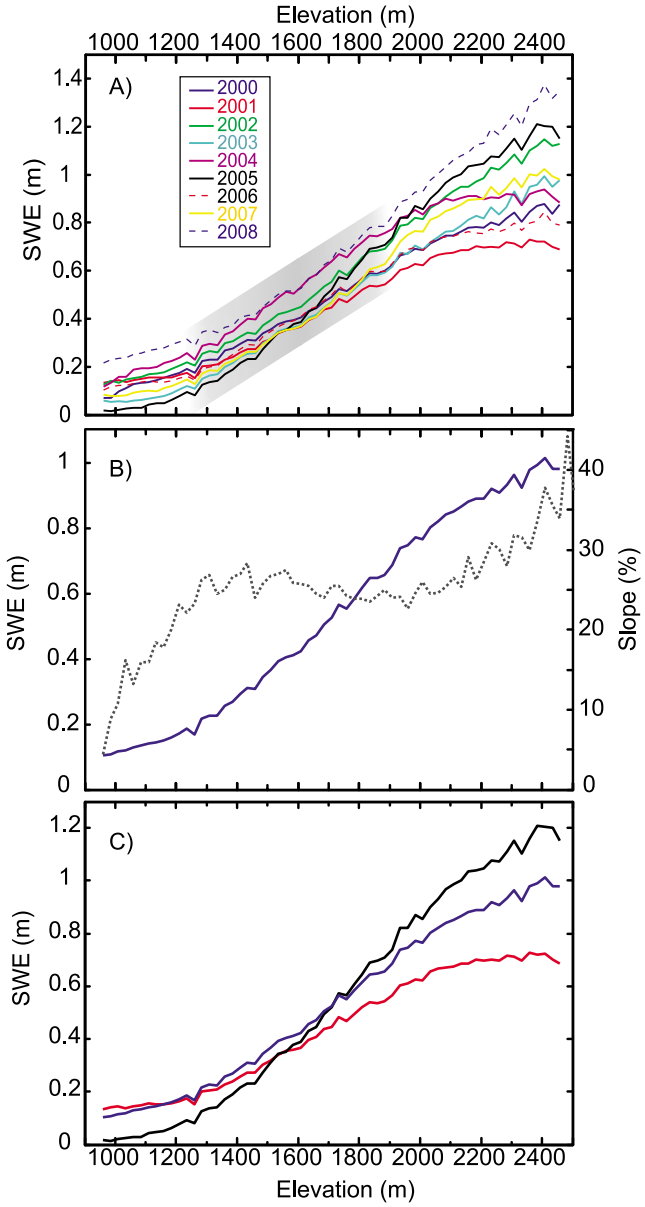

Figure 7. SWE versus elevation. (a) Lines show model-generated total SWE by elevation band; gray box shows the elevation range ~1200 m to ~2000 m where curves are approximately linear. The three zones of SWE lapse rates referred to in the text can be seen here: the low-elevation zone extends from the valley floors to ~1200 m, the midelevation zone from ~1200 m to ~2000 m, and the high-elevation zone extends above ~2000 m. Data do not extend above 2500 m because too few pixels exist for adequate portrayal of elevation bands. (b) Average slope by elevation (dotted gray line). (c) The 2001 (red line) and 2005 (black line) average total SWE by elevation. Blue line is average total SWE by elevation (2000–2008) in both Figures 7b and 7c.

characteristic temperature noise completely encompasses this difference showing that the day of melt can range over a very large number of days.

[35] Under present conditions and projected future warmer conditions, the high-frequency component (i.e., Figure 5b; the daily deviations from seasonal trend) of natural temperature variability alone does not affect the timing of snowmelt as severely as characteristic noise containing both low- and high-frequency temperature variations. The high-frequency noise varied modern snowmelt timing by an average of 15 days. Under a warmer climate, however, high-frequency noise has a greater impact on snowmelt timing with a variability of 17 days.

[36] Although the differences in melt timing between years of low and high snow for present and future conditions are not significant, there are substantial differences between present and future melt timing for both the low- and high-snow scenarios. On average, future melt arrives 19–26 days earlier depending on percentile (Table 3 and Figure 10). The amount of overlap of the modern and future pdfs in a given scenario gives us a measure of the overlap of melt conditions expected in the future. For the low-snow scenario, there is only about 10% overlap between present and future conditions. For the high-snow scenario, there is more overlap, but still mostly less than 25%. We combine the three melt percentiles to give an overall measure of the shift in melt timing in the future with respect to an arbitrary modern-day melt percentile (Table 3 and Figure 11). Our results indicate that a spread of over 4 weeks in melt timing exists because of temperature noise, but on average, future melting occurs 21.5 days earlier. These measures show that we can expect future melt to occur about 3 weeks earlier, but with some overlap with present conditions because of the extreme range in melt timing due to temperature variability.

4. Discussion

[37] The close correspondence between three different accumulated SWE lapse rates and three zones of topography (Figure 7b) gives some important insight into mountain snowfall processes. The low-elevation zone shows a very small SWE lapse rate while the topography steepens rapidly. The midelevation zone exhibits a constant linear SWE lapse rate across topography where slopes remain relatively constant. This zone encompasses most of the area of the basin. The highest elevations show a reduction in the SWE lapse rate coincident with rapidly steepening topography. Our modeling observations of the low-elevation zone imply that orographic processes are not important at low elevation in this basin because storm events are relatively uniform between locations at and near the valley floor. In midelevation zones, orographic processes dominate to yield a nearly linear, steep increase in snowfall with elevation. At high elevations, precipitation is known to diminish due to depletion of orographically lifted air masses [*Choularton and Perry*, 1986] and can approach zero if relief is high enough [e.g., *Harper and Humphrey*, 2003]. Also likely playing a part in the reduction of the SWE lapse rate in the high-elevation zone is the redistribution of snow by wind and perhaps higher sublimation on blocky alpine slopes [*Liston and Sturm*, 1998].

[38] Our results offer a means to test the ability of sparse snow measurements to characterize the overall snow quantity in a large mountain basin. There are nine SNOTEL sites in 24,000 km^2 surrounding the MF basin. These are between 1326 m to 2103 m elevation, only two are within the basin and both of these are near the basin boundary. We find that the sampling locations in and around the MF basin fail to adequately detect a large fraction of SWE. The highest

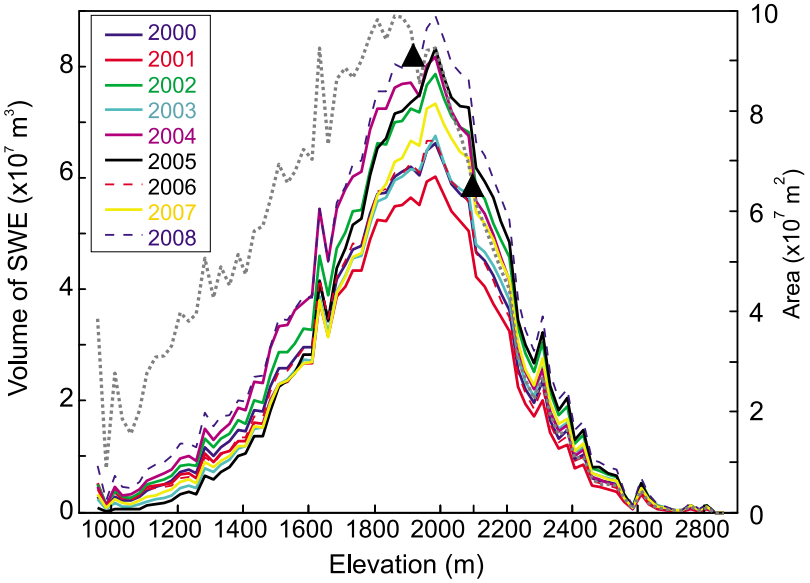

Figure 8. Volume of total SWE accumulated each of the study years (colored lines). Gray dotted line shows the area versus elevation of the basin, and black triangles represent the elevation of the Badger Pass (higher) and Flattop Mountain (lower) SNOTEL stations.

SNOTEL sits at 2103 m (which is anomalously high for the region) with only about 15% of basin area higher. Yet, over 25% of the annual SWE accumulates above this measuring station. Over half of the annual SWE accumulates on 33% of the total basin area that exists above the second highest SNOTEL site in the region. A significant 71% of SWE accumulates in the MF basin above the mean elevation of surrounding monitoring stations (Table 2). We find the strongest disconnect between basin area and snow volume in the 2000–2200 m elevation range (Figure 12).

[39] An understanding of SWE lapse rates is important for upscaling point measurements to the basin. The 9 year average SWE lapse rate for the midelevation region (~1200 to 2000 m) is 7.88×10^{-4} m of SWE increase with each m of elevation gain (Table 2). However, the individual years of 2001 and 2005 varied from 6.17×10^{-4} m/m to 10.41×10^{-4}

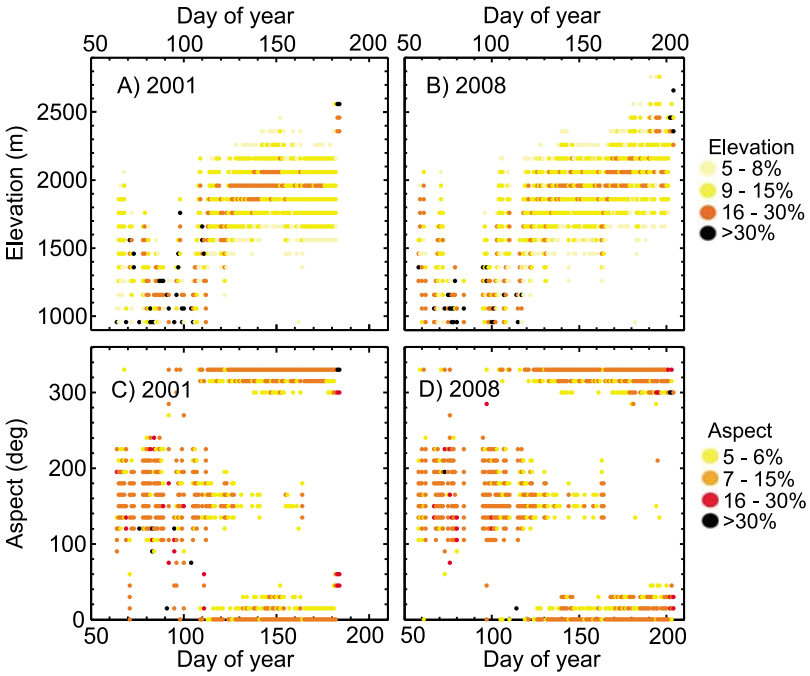

Figure 9. Modeled time-space distribution of snowmelt. (a and b) Percent of total daily melt by elevation. Each dot shows percent of total basin melt for a particular day occurring at each elevation band. (c and d) Same as in Figures 9a and 9b, but for aspect where north is 0°, east is 90°, south is 180°, and west is 270°. Low-snow year (2001) and high-snow year (2008) are shown. Values of less than 5% are not shown.

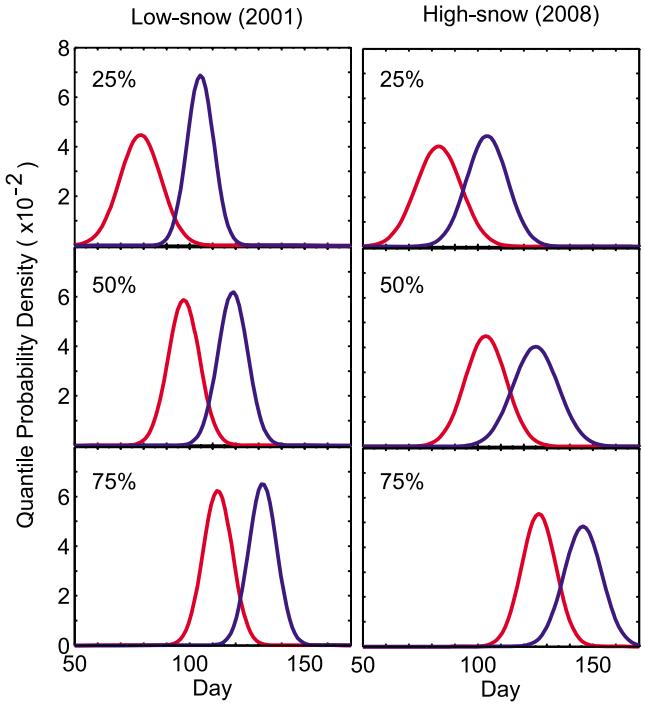

Figure 10. Time probability distribution functions (pdfs) of snowmelt. Plots show pdfs derived from 100 simulation runs with random variability of temperature. Three percentiles of basin snowmelt are displayed for both high- and low-snow years: The pdf for 25% of total basin SWE melted; The pdf for 50% of basin SWE melted, and the pdf for 75% of basin SWE melted. Blue lines represent modern-day simulations, and red lines represent simulations under projected future warming scenario (2070–2099).

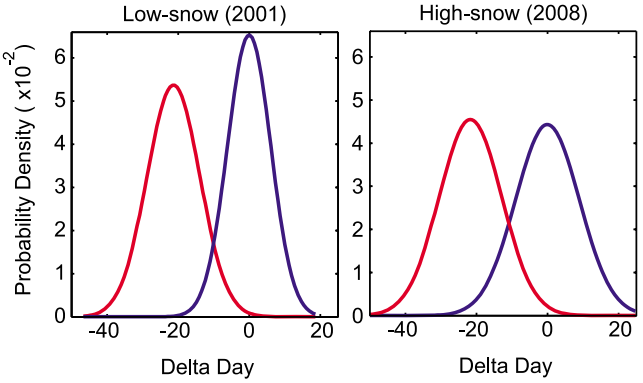

Figure 11. Probability distribution functions from combining the percentiles of melt for each characteristic temperature scenario. Results are centered about the mean of the modern scenario with deviations from the mean represented as delta day. Blue lines represent modern-day scenarios, and red lines represent projected future warming scenarios (2070–2099).

m/m, respectively, a 60% difference in the gradient (Figure 7c). The low-elevation total accumulated SWE was near average in 2001, but there was a shallow SWE lapse rate and below average SWE at midrange to higher elevations. In contrast, the low-elevation total accumulated SWE was far below average in 2005, but there was a steep SWE lapse rate and large accumulation at high elevations. Hence, analysis of the snowpack below 1600 m would erroneously lead one to believe that in 2001 basin SWE was greater than in 2005. Fortunately, the consistently linear lapse rate across the midelevation range means that SWE can be estimated for this zone from the gradient derived from only two points, assuming spatially representative samples can be obtained for an entire elevation band. While we believe our results provide the best available information on SWE lapse rates, we reiterate that care must be taken in adopting our interpretation

Table 3. Simulation Results of Characteristic Noise Scenarios for the Low-Snow and High-Snow Seasons[a]

	Modern			Future			Days Earlier[d]	Overlap[e] (%)
	Mean	σ[b]	Spread[c]	Mean	σ[b]	Spread[c]		
				Individual Percentile PDFs				
Low Snow								
25%	104.7	5.80	23.2	78.7	8.92	35.7	26	7.5
50%	118.8	6.45	25.8	97.5	6.79	27.2	21.3	10.8
75%	131.8	6.12	24.5	112.2	6.38	25.5	19.6	11.7
Mean		*6.12*	*24.5*		*7.36*	*29.5*	*22.3*	*10.0*
High Snow								
25%	104.0	8.91	35.6	83.0	9.84	39.4	21	26.2
50%	125.1	9.89	39.6	103.4	8.95	35.8	21.7	24.9
75%	145.6	8.23	32.9	126.5	7.45	29.8	19.1	22.3
Mean		*9.01*	*36.0*		*8.75*	*35.0*	*20.6*	*24.5*
Overall Mean		**7.57**	**30.3**		**8.06**	**32.3**	**21.5**	
				Combined PDFs[f]				
Low Snow	0	6.11	24.4	−21.29	7.43	29.7	21.3	11.5
High Snow	0	9.00	36.0	−21.66	8.77	35.1	21.7	22.3
Mean		7.56	30.2		8.10	32.4	21.5	

[a]Numbers in italic are the mean of the above column, while bold values are the overall mean.
[b]One standard deviation of 100 simulation runs.
[c]The total number of days within ±2 σ of the mean.
[d]The difference in the mean day of the modern and future pdf.
[e]"Overlap" is a measure of the number of days the future probability distribution functions occupy in common with the modern probability distribution functions (pdfs).
[f]Combined pdf results displays the variability and overlap of all three percentiles in one pdf with the mean of the modern-day scenario centered at zero.

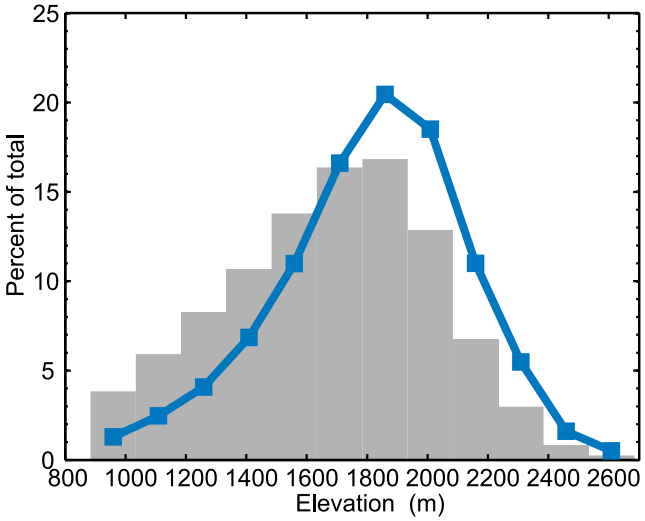

Figure 12. Basin area (gray bars) by elevation and basin SWE volume (blue line) by elevation as a percent of the total. SWE is averaged over the 9 years of record 2000–2008.

because an elevation-dependent scheme was used to generate these gradients and no independent verification is available.

[40] In portions of the Swiss Alps, modeling has suggested that snowmelt will produce a large but short runoff peak under a warming climate [*Bavay et al.*, 2009]. Recent studies of western United States mountains have concluded that over the last 50 years the timing of snowmelt has shifted toward earlier in the year by days to weeks in many areas of the west, although not all [*McCabe and Clark*, 2005; *Moore et al.*, 2007; *Regonda et al.*, 2005; *Stewart et al.*, 2005]. The latter studies are based on trends in the inferred timing of some quantity of melt, for example the center of mass of river discharge (approximately equivalent to our 50th percentile). Since any given year has just one snowpack and climate, the role of noise in the climate system in dictating the timing of snowmelt is not easily isolated by analysis of historical data. Of interest is the significance of a shift relative to the natural range of the system: how conditions, which were once rare, become common. Our simulations imply a 4 week spread in snowmelt timing due to climate noise under present conditions. This large range means that time shifts in melt caused by future warming of days to weeks will still have considerable overlap with present-day conditions (Figure 11). It is important to emphasize that our measures of "overlap" describe a low-snow year today and in the future, and likewise a high-snow year today and in the future. Consequently, an entire measure of overlap for all varieties of snow years today and in the future is not addressed and is likely significantly higher.

[41] Further, our simulations show that high-snow years don't simply shift the timing of snowmelt percentiles later in the year, but that the range of possible days for achieving a particular percentile of melt is expanded during a high-snow year. With a larger amount of snow and thus slower melt out, a high-snow year effectively has more degrees of freedom with respect to melt timing than a low-snow year. This demonstrates that the timing of snowmelt runoff is closely tied to precipitation. Accordingly, in both historical trend analysis and in future projections, the impacts of precipitation on timing must be compensated for. Importantly, we have only modeled the generation of snow meltwater and not processes related to the routing of water to streams.

5. Conclusions

[42] The results of this work imply that a large fraction of the total SWE in mountainous basins is not sampled by existing ground measurements. Importantly, this snow is at high elevation where it will likely continue to snow even under warmer conditions. Results also revealed that the vertical gradient of SWE accumulation varies considerably from year-to-year, showing that point measurements cannot be scaled to basin SWE with a simple transfer function. Both of these factors heavily influence the outcomes of long-term trend analysis studies in this sparsely instrumented region. Second, we have investigated the effects of natural temperature variability on the melt of high-elevation snowpacks. Our results indicate that temperature variability alone can impact the timing of snowmelt percentiles by 4 weeks, with wetter years having a larger range than drier years. Further, temperature related climate noise plays a larger role on snowmelt timing in a warmer climate. Due to the variability inherent in snowmelt due to characteristic noise related to daily and multiday cold/warm spells, snowmelt conditions in a warmer climate will sometimes overlap those that we experience today, but will on average occur ~3 weeks earlier than present.

[43] While these results are based on many simplifying assumptions, they serve as a starting point for quantifying the effects of climate change on our current snow conditions and possible simulation of those effects in the future. This is a much more robust approach than projecting trends from fitting past data because it incorporates fundamental properties of the basin and snowpack as well as system noise. The numerical results presented here are specific to the MF basin, but the main ideas should be applicable to most snowmelt-dominated watersheds in the Northern Rocky Mountains or other Cordillera with similar climates.

[44] **Acknowledgments.** This work is funded by NSF-Hydrological Sciences EAR-0609570, CUAHSI-Hydrologic Observatory CFDA 47.050, and a Montana Space Grant Consortium Fellowship. We thank three anonymous reviewers for constructive comments which improved this manuscript.

References

Ault, T. W., K. P. Czajkowski, T. Benko, J. Coss, J. Struble, A. Spongberg, M. Templin, and C. Gross (2006), Validation of the MODIS snow product and cloud mask using student and NWS cooperative station observations in the lower Great Lakes region, *Remote Sens. Environ.*, *105*, 341–353, doi:10.1016/j.rse.2006.07.004.

Bales, R. C., N. P. Molotch, T. H. Painter, M. D. Dettinger, R. Rice, and J. Dozier (2006), Mountain hydrology of the western United States, *Water Resour. Res.*, *42*, W08432, doi:10.1029/2005WR004387.

Barnett, T. P., et al. (2008), Human-induced changes in the hydrology of the western United States, *Science*, *319*(5866), 1080–1083, doi:10.1126/science.1152538.

Bavay, M., M. Lehning, T. Jonas, and H. Lowe (2009), Simulations of future snow cover and discharge in Alpine headwater catchments, *Hydrol. Processes*, *23*(1), 95–108, doi:10.1002/hyp.7195.

Bleha, J. A., and J. T. Harper (2007), Snowmelt water generation in a large mountain basin of northwest Montana from a MODIS driven model, in *Proceedings of Symposium on Environmental Sensing*, pp. 83–86, Inland Northwest Res. Alliance Inc., Boise, Idaho.

Bohr, G. S., and E. Aguado (2001), Use of April 1 SWE measurements as estimates of peak seasonal snowpack and total cold-season precipitation, *Water Resour. Res.*, *37*, 51–60, doi:10.1029/2000WR900256.

Cayan, D. R. (1996), Interannual climate variability and snowpack in the western United States, *J. Clim.*, *9*(5), 928–948, doi:10.1175/1520-0442(1996)009<0928:ICVASI>2.0.CO;2.

Choularton, R. W., and S. J. Perry (1986), A model of the orographic enhancement of snowfall by the seeder-feeder mechanism, *Q. J. R. Meteorol. Soc.*, *112*, 335–345, doi:10.1002/qj.49711247204.

Cline, D. W., and T. R. Carroll (1999), Inference of snow cover beneath obscuring clouds using optical remote sensing and a distributed snow energy and mass balance model, *J. Geophys. Res.*, *104*(D16), 19,631–19,644, doi:10.1029/1999JD900249.

Deems, J. S., S. R. Fassnacht, and K. J. Elder (2006), Fractal distribution of snow depth from lidar data, *J. Hydrometeorol.*, *7*(2), 285–297, doi:10.1175/JHM487.1.

Dodson, R., and D. Marks (1997), Daily air temperature interpolated at high spatial resolution over a large mountainous region, *Clim. Res.*, *8*, 1–20, doi:10.3354/cr008001.

Elder, K., J. Dozier, and J. Michaelsen (1991), Snow accumulation and distribution in an alpine watershed, *Water Resour. Res.*, *27*, 1541–1552, doi:10.1029/91WR00506.

Fassnacht, S. R., K. A. Dressler, and R. C. Bales (2003), Snow water equivalent interpolation for the Colorado River Basin from snow telemetry (SNOTEL) data, *Water Resour. Res.*, *39*(8), 1208, doi:10.1029/2002WR001512.

Hall, D. K., and G. A. Riggs (2007), Accuracy assessment of the MODIS snow products, *Hydrol. Processes*, *21*(12), 1534–1547, doi:10.1002/hyp.6715.

Hall, D. K., G. A. Riggs, and V. V. Salomonson (2006), MODIS/Terra snow cover 8-Day L3 global 500m grid V005, February 2000 to September 2008, http://nsidc.org/data/mod10a2v5.html, Natl. Snow and Ice Data Cent., Boulder, Colo. (Updated daily/weekly.)

Hamlet, A. F., and D. P. Lettenmaier (2007), Effects of 20th century warming and climate variability on flood risk in the western U.S., *Water Resour. Res.*, *43*, W06427, doi:10.1029/2006WR005099.

Harper, J. T., and N. F. Humphrey (2003), High altitude Himalayan climate inferred from glacial ice flux, *Geophys. Res. Lett.*, *30*(14), 1764, doi:10.1029/2003GL017329.

Hock, R. (1999), A distributed temperature-index ice- and snowmelt model including potential direct solar radiation, *J. Glaciol.*, *45*(149), 101–111.

Hock, R. (2003), Temperature index melt modeling in mountain areas, *J. Hydrol.*, *282*, 104–115, doi:10.1016/S0022-1694(03)00257-9.

Intergovernmental Panel on Climate Change (IPCC) (2007), *Climate Change 2007*: The Physical Science Basis: Contribution of Working Group I to the Fourth Assessment Report of the IPCC, edited by S. Solomon et al., Cambridge Univ. Press, New York.

Julander, R. P., and M. Bricco (2006), An examination of external influences embedded in the historical snow data of Utah, paper presented at 74th Annual Meeting, Western Snow Conf., Las Cruces, N. M.

Klein, A. G., D. K. Hall, and G. A. Riggs (1998), Improving snow cover mapping in forests through the use of a canopy reflectance model, *Hydrol. Processes*, *12*(10–11), 1723–1744, doi:10.1002/(SICI)1099-1085(199808/09)12:10/11<1723::AID-HYP691>3.0.CO;2-2.

Knowles, N., M. D. Dettinger, and D. R. Cayan (2006), Trends in snowfall versus rainfall in the western United States, *J. Clim.*, *19*(18), 4545–4559, doi:10.1175/JCLI3850.1.

Kuhn, M. (1987), Micro-meteorological conditions for snow melt, *J. Glaciol.*, *33*(113), 263–272.

Liston, G. E., and M. Sturm (1998), A snow-transport model for complex terrain, *J. Glaciol.*, *44*(148), 498–516.

McCabe, G. J., and M. P. Clark (2005), Trends and variability in snowmelt runoff in the western United States, *J. Hydrometeorol.*, *6*(4), 476–482, doi:10.1175/JHM428.1.

Meehl, G. A., C. Covey, T. Delworth, M. Latif, B. McAvaney, J. F. B. Mitchell, R. J. Stouffer, and K. E. Taylor (2007), The WCRP CMIP3 multi-model dataset: A new era in climate change research, *Bull. Am. Meteorol. Soc.*, *88*, 1383–1394, doi:10.1175/BAMS-88-9-1383.

Molotch, N. P. (2009), Reconstructing snow water equivalent in the Rio Grande headwaters using remotely sensed snow cover data and a spatially distributed snowmelt model, *Hydrol. Processes*, *23*(7), 1076–1089, doi:10.1002/hyp.7206.

Molotch, N. P., and R. C. Bales (2005), Scaling snow observations from the point to the grid element: Implications for observation network design, *Water Resour. Res.*, *41*, W11421, doi:10.1029/2005WR004229.

Molotch, N. P., and R. C. Bales (2006), SNOTEL representativeness in the Rio Grande headwaters on the basis of physiographics and remotely sensed snow cover persistence, *Hydrol. Processes*, *20*(4), 723–739, doi:10.1002/hyp.6128.

Molotch, N. P., S. R. Fassnacht, R. C. Bales, and S. R. Helfrich (2004), Estimating the distribution of snow water equivalent and snow extent beneath cloud cover in the Salt-Verde River basin, Arizona, *Hydrol. Processes*, *18*(9), 1595–1611.

Moore, J. N., J. T. Harper, and M. C. Greenwood (2007), Significance of trends toward earlier snowmelt runoff, Columbia and Missouri Basin headwaters, western United States, *Geophys. Res. Lett.*, *34*(16), L16402, doi:10.1029/2007GL031022.

Mote, P. W. (2006), Climate-driven variability and trends in mountain snowpack in western North America, *J. Clim.*, *19*(23), 6209–6220, doi:10.1175/JCLI3971.1.

NOHRSC (2004), Snow Data Assimilation System (SNODAS) data products at NSIDC, http://nsidc.org/data/g02158.html, Natl. Snow and Ice Data Cent., Boulder, Colo.

Palmer, P. L. (1988), The SCS snow survey water supply forecasting program: Current operations and future directions, paper presented at 56th Annual Meeting, Western Snow Conf., Kalispell, Mont.

Parajka, J., and G. Blöschl (2008), Spatio-temporal combination of MODIS images: Potential for snow cover mapping, *Water Resour. Res.*, *44*, W03406, doi:10.1029/2007WR006204.

Pellicciotti, F., B. Brock, U. Strasser, P. Burlando, M. Fund, and J. Corripio (2005), An enhanced temperature-index glacier melt model including the shortwave radiation balance: Development and testing for Haut Glacier d'Arolla, Switzerland, *J. Glaciol.*, *51*(175), 573–587, doi:10.3189/172756505781829124.

Regonda, S. K., B. Rajagopalan, M. Clark, and J. Pitlick (2005), Seasonal cycle shifts in hydroclimatology over the western United States, *J. Clim.*, *18*(2), 372–384, doi:10.1175/JCLI-3272.1.

Salomonson, V. V., and I. Appel (2004), Estimating fractional snow cover from MODIS using the normalized difference snow index, *Remote Sens. Environ.*, *89*, 351–360, doi:10.1016/j.rse.2003.10.016.

Salomonson, V. V., and I. Appel (2006), Development of the Aqua MODIS NDSI fractional snow cover algorithm and validation results, *IEEE Trans. Geosci. Remote Sens.*, *44*(7), 1747–1756, doi:10.1109/TGRS.2006.876029.

Savitzky, A., and M. Golay (1964), Smoothing and differentiation of data by simplified least squares procedures, *Anal. Chem.*, *36*, 1627–1639, doi:10.1021/ac60214a047.

Serreze, M. C., M. P. Clark, R. L. Armstrong, D. A. McGinnis, and R. S. Pulwarty (1999), Characteristics of the western United States snowpack from snowpack telemetry (SNOTEL) data, *Water Resour. Res.*, *35*, 2145–2160, doi:10.1029/1999WR900090.

Simic, A., R. Fernandes, R. Brown, P. Romanov, and W. Park (2004), Validation of VEGETATION, MODIS, and GOES + SSM/I snow-cover products over Canada based on surface snow depth observations, *Hydrol. Processes*, *18*(6), 1089–1104, doi:10.1002/hyp.5509.

Stewart, I. T., D. R. Cayan, and M. D. Dettinger (2005), Changes toward earlier streamflow timing across western North America, *J. Clim.*, *18*(8), 1136–1155, doi:10.1175/JCLI3321.1.

Taaheri, A., Y. Liu, and A. Cohen (2007), HDF-EOS to GeoTiff conversion tool (HEG) stand-alone user's guide, version 2.8r5, technical paper, NASA, Upper Marlboro, Md.

Westerling, A. L., H. G. Hidalgo, D. R. Cayan, and T. W. Swetnam (2006), Warming and earlier spring increase western U.S. forest wildfire activity, *Science*, *313*(5789), 940–943, doi:10.1126/science.1128834.

Zhou, X., H. Xie, and J. M. H. Hendrickx (2005), Statistical evaluation of remotely sensed snow-cover products with constraints from streamflow and SNOTEL measurements, *Remote Sens. Environ.*, *94*, 214–231, doi:10.1016/j.rse.2004.10.007.

B. J. Gillan, J. T. Harper, and J. N. Moore, Department of Geosciences, University of Montana, 32 Campus Dr., Missoula, MT 59812, USA. (Joel@mso.umt.edu)